Versatile ytterbium ion trap experiment for operation of scalable ion-trap chips with motional heating and transition-frequency measurements

James J. McLoughlin, Altaf H. Nizamani, James D. Siverns, Robin C. Sterling, Marcus D. Hughes, Bjoern Lekitsch, Björn Stein, Seb Weidt, and Winfried K. Hensinger*

Department of Physics and Astronomy, University of Sussex, Brighton BN1 9QH, United Kingtom

(Received 22 July 2010; published 21 January 2011)

We present the design and operation of an ytterbium ion trap experiment with a setup offering versatile optical access and 90 electrical interconnects that can host advanced surface and multilayer ion trap chips mounted on chip carriers. We operate a macroscopic ion trap compatible with this chip carrier design and characterize its performance, demonstrating secular frequencies >1 MHz, and trap and cool nearly all of the stable isotopes, including $^{171}Yb^+$ ions, as well as ion crystals. For this particular trap we measure the motional heating rate $\langle\dot{n}\rangle$ and observe an $\langle\dot{n}\rangle \propto 1/\omega^2$ behavior for different secular frequencies ω. We also determine a spectral noise density $S_E(1\ \text{MHz}) = 3.6(9) \times 10^{-11}\ \text{V}^2\ \text{m}^{-2}\ \text{Hz}^{-1}$ at an ion electrode spacing of 310(10) μm. We describe the experimental setup for trapping and cooling Yb^+ ions and provide frequency measurements of the $^2S_{1/2} \leftrightarrow {}^2P_{1/2}$ and $^2D_{3/2} \leftrightarrow {}^3D[3/2]_{1/2}$ transitions for the stable $^{170}Yb^+$, $^{171}Yb^+$, $^{172}Yb^+$, $^{174}Yb^+$, and $^{176}Yb^+$ isotopes which are more precise than previously published work.

DOI: 10.1103/PhysRevA.83.013406 PACS number(s): 37.10.Ty, 32.30.Jc, 03.67.Lx, 07.30.Kf

I. INTRODUCTION

Ions confined in radio-frequency (rf) traps are regarded as one of the most promising approaches to quantum information processing [1–3], as well as for quantum simulators [4–8] and frequency standards [9–12]. Their suitability has been well demonstrated with state preparation and detection [13–17]; qubit entanglement, gates, and error correction [18–27]; and transport of ions within ion trap arrays [28–36]. Development of scalable traps that can encompass all of these operations is now the next stage toward more practical systems incorporating microfabricated chip traps [36–47], but realizing experimental setups can be challenging. We have developed an experiment honed toward the development of trap architectures which includes a vacuum system that accommodates both surface and multilayer traps and provides up to 90 electrical connections enabling the design and testing of a wide range of complex trap geometries to be mounted on commercial compatible chip carriers. We discuss the experimental setup, particularly describing the vacuum system and laser locking and imaging devices used. We describe a macroscopic ion trap compatible with chip carrier mounting and characterize its operation. Noise such as electric field fluctuations (from thermal electric Johnson-Nyquist noise) and fluctuating patch potentials on electrodes induces motional heating of trapped ions [44,48–50]. We measure the motional heating rate within our ion trap using a technique where the laser cooling beam is turned off for a certain time and ion fluorescence is monitored when the laser is turned on again [51,52]. There are currently several ions being investigated for quantum technology including Ba^+ [53], Be^+ [54], Ca^+ [55–59], Cd^+ [60], Mg^+ [61], Sr^+ [32,62], and Yb^+ [63–66]. Yb^+ is an attractive choice for quantum information processing and for frequency standards [67–70]. We present frequency measurements more precise than previously published results [71] for the $^2S_{1/2} \leftrightarrow {}^2P_{1/2}$ transition and the $^2D_{3/2} \leftrightarrow {}^3D[3/2]_{1/2}$ for the Yb^+ isotopes: $^{170}Yb^+$, $^{171}Yb^+$, $^{172}Yb^+$, $^{174}Yb^+$, and $^{176}Yb^+$.

II. EXPERIMENTAL SETUP

Our vacuum system has some similar features to the one used in Ref. [37] and includes a custom mounting bracket with 90 electrical connections, four atomic ovens, and versatile optical access to cater to traps that require laser access via a through hole and traps that require laser beams parallel to the surface of the trap. The mounting bracket, shown in Fig. 1, consists of two ultra-high vacuum (UHV) compatible polyether ether ketone (PEEK) plates sandwiching 90 gold-plated receptacles (Mill-Max; 0672-1-15-15-30-27-10-0) which are arranged to be compatible with 101-pin CPGA chip carriers (Global Chip Material; part no. PGA10047002). This setup enables complex trap structures that are mounted on chip carriers to be easily inserted into the mounting bracket and changed with minimal turnaround time. Kapton insulated copper wires connect 88 receptacles to two 50-pin feedthroughs providing control of the ion trap static-voltage electrodes. Two receptacles are used for rf and grounding and are connected to a power feedthrough (Kurt J. Lesker; EFT0521052) with a pair of short, thick, bare copper wires insulated with ceramic beads.

Groove grabbers attach the mounting bracket to a vacuum chamber, comprised of an octagon and a hemisphere (Kimball Physics; part nos. MCF450-SO20008-C and MCF450-MH10204/8-A, respectively), as shown in Fig. 2. Four atomic ovens (ohmically heated stainless-steel tubes) are arranged in the chamber to provide the surface and multilayer traps with either natural ytterbium or an enriched source of ^{171}Yb atoms. Eight 1.33-in. conflat (CF) mounted antireflection (AR) coated fused quartz silica viewports allow laser access to the center of both trap types, and a specially designed 4.5-in., CF mounted, AR coated re-entrant window is mounted in front of the chamber to allow imaging of the ion. The distance between the ion and the window surface is 4 mm. A UHV environment of 10^{-12} Torr is accomplished using

*W. K. Hensinger@sussex.ac.uk; URL: http://www.sussex.ac.uk/physics/iqt

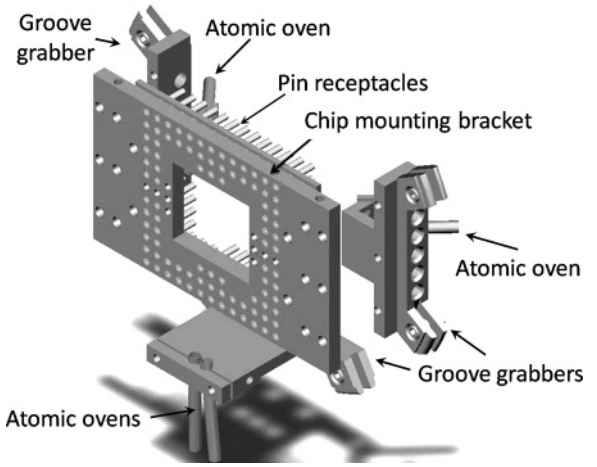

FIG. 1. View of the mounting bracket showing the 90 pin receptacles and the positions of the four atomic ovens. Two ovens are behind the pins and angled to provide ytterbium atoms to multilayer ion traps featuring a through hole. The other two ovens provide atoms for traps where access is parallel to the ion trap surface.

a 20 ls^{-1} ion pump (Varian; part no. 9191145) and titanium sublimation pump (Varian; part no. 9160050).

The rf drive frequency is generated using an HP8640B signal generator, amplified (NP Technologies no. NP-541), and passed through a resonator [72,73], which is then attached to the power feedthrough. The resonator design specifications are detailed in Table I and, when loaded with the trap, has a quality factor $Q = 200(20)$ and geometric factor $\kappa = 24(8)$, defined by $V = \kappa\sqrt{PQ}$, where V is the rf voltage applied to the electrodes, P the power applied to the electrodes, and Q the quality factor of the resonator [73]. Impedance matching is achieved by measuring the percentage of reflected power to applied power using a directional power meter (Rhode and Schwarz; part no. NAUS 3), and the coupling is maintained at $\geqslant 95\%$.

The macroscopic linear rf Paul trap used is shown in Fig. 3. To be compatible with the vacuum system it is limited to a footprint of 3 × 3 cm, and a height of 1 cm, and can be plugged

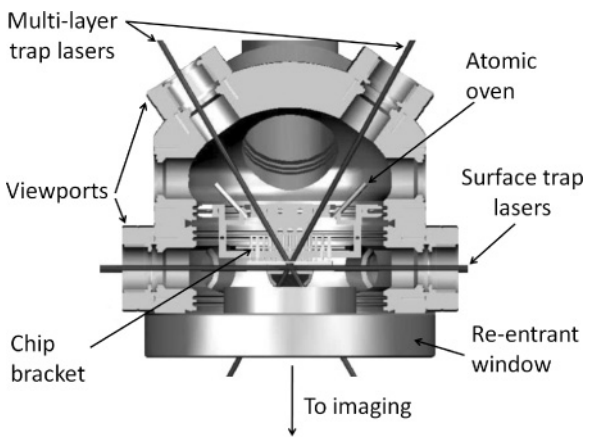

FIG. 2. Top cut-view of the vacuum chamber (consisting of an octagon and a hemisphere flange) showing the mounting bracket, atomic ovens, and laser access for symmetric and surface traps.

TABLE I. Specifications of the resonator.

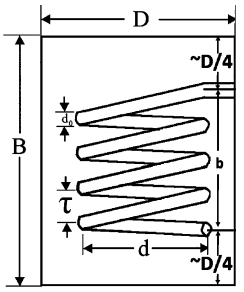

Shield diameter D	76(1) mm
Shield length B	103(1) mm
Coil diameter d	52(3) mm
Coil length b	63(5) mm
Coil diameter d_0	3.14(3) mm
Winding pitch τ	6(2) mm
Number of turns	9.50(25)
Resonant frequency with trap load, f_0	21.5(1) MHz
Q with trap load	200(20)

into the mounting bracket. A PEEK base is used to avoid electrical shorting with the mounting bracket connections. Exposure to laser radiation has been observed to increase outgassing and induce discoloring of PEEK. This is suspected to cause charging of the dielectric, so a stainless-steel mount is used to shield the ion from any exposed dielectrics. Blade-shaped electrodes, electroplated with 5 μm gold, are suspended from the stainless-steel mount. The rf electrodes span the entire axial length of the trap, while the static-voltage electrodes are segmented to provide end-cap potentials and rotation of the principal axes. This arrangement provides for a reduced residual rf ponderomotive potential along the z axis [74] to <2% of the radial frequency and allows trapping of long ion chains without appreciable rf micromotion in the axial

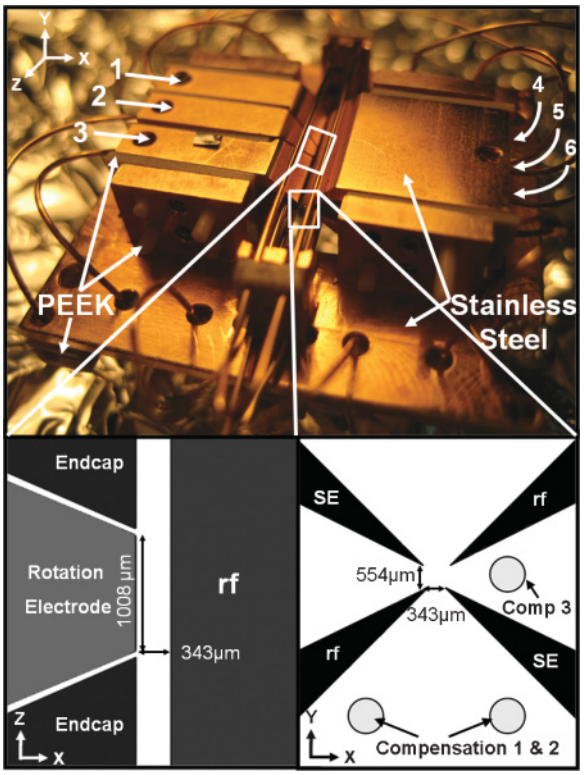

FIG. 3. (Color online) Top: Ion trap used in experiments. Bottom right: Cross-sectional view of the radial plane of the trap, showing the spacings between the radio frequency (rf) electrodes and the static-voltage electrodes (SE). Bottom left: View of the trap showing the length of the center electrode and trapping region.

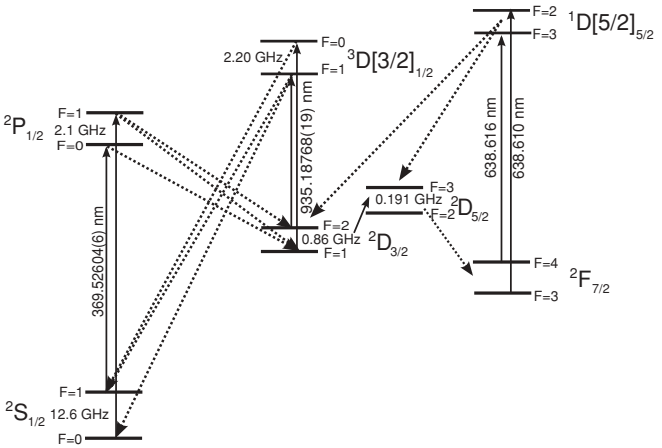

FIG. 4. Energy level scheme for $^{171}Yb^+$, where the ground-state hyperfine levels $^2S_{1/2}|F=0, m_F=0\rangle$ and $^2S_{1/2}|F=1, m_F=0\rangle$ represent the qubit states $|0\rangle$ and $|1\rangle$, respectively. The $^2S_{1/2} \leftrightarrow {}^2P_{1/2}$, used for Doppler cooling and fluorescence detection, is driven by a 369.5-nm beam with 14.7-GHz-frequency sidebands. Decay from the $^2P_{1/2}$ state to the metastable $^2D_{3/2}$ state is returned to the ground state by exciting the $^2D_{3/2} \leftrightarrow {}^3D[3/2]_{1/2}$ transition using a 935.2-nm beam with 3.08-GHz-frequency sidebands. The $^2F_{7/2}$ state is populated a few times per hour and the ion is returned to the ground state using a 638.6-nm laser switched between the two $^2F_{7/2} \leftrightarrow {}^1D[5/2]_{5/2}$ transitions. Wavelength values (vacuum) are shown.

direction. The electrodes are separated by 343(14) μm on the x axis and 554(14) μm on the y axis, producing a trap aspect ratio of 1.6, and the ion-electrode separation is 310(10) μm. The length of the center electrode is 1008(14) μm. Three parallel wires, compensation electrodes 1–3, run the length of the trap to provide micromotion compensation. Holes in the mount coincide with respective receptacles in the mounting bracket, and gold-plated wires connect the electrodes to the pin receptacles.

To create Yb^+ ions neutral atoms are directed toward the center of a trapping region and ionized using two-color photoionization [64]. Here a 398.9-nm photon excites the neutral $^1S_0 \leftrightarrow {}^1P_1$ transition, with a subsequent 369.5-nm photon ionizing the atom. Figure 4 shows the energy level diagram for $^{171}Yb^+$, with the hyperfine doublets resulting from the ion's spin-1/2 nucleus. The ground-state levels, $^2S_{1/2}|F=0, m_F=0\rangle$ and $^2S_{1/2}|F=1, m_F=0\rangle$, represent the qubit states $|0\rangle$ and $|1\rangle$, respectively. The stable isotopes $^{170}Yb^+$, $^{172}Yb^+$, $^{174}Yb^+$, and $^{176}Yb^+$ have zero nuclear spin, resulting in similar energy level structures but without a hyperfine structure.

$^{171}Yb^+$ ions are Doppler cooled on the 369.5-nm $^2S_{1/2} \leftrightarrow {}^2P_{1/2}$ electric dipole transition (natural linewidth $\Gamma/2\pi = 19.6$ MHz [75]). The 369.5-nm beam, with 14.7-GHz-frequency sidebands used to repump hyperfine states, is generated by frequency doubling a 7.35-GHz, phase-modulated (New Focus electro-optic modulator no. 4851), 739.05-nm beam in a resonant doubling cavity (Toptica Photonics TA-SHG, with a free spectral range of 1.05 GHz).

The $^2P_{1/2}$ state decays (branching ratio $\approx$0.005 [66]) to the metastable $^2D_{3/2}$ state (lifetime $\tau = 52$ ms [76]). A 935.2-nm laser, current modulated at 3.08 GHz using a bias-t (Mini Circuits; part no. ZFBT-4R2G+), excites transitions to the $^3D[3/2]_{1/2}$ state, allowing rapid population of the ground state. Inelastic collisions with background gas ($\approx$30 min) results in population of the $^2F_{7/2}$ state (natural lifetime of $\approx$6 years [70]). A laser scanned between 638.610 and 638.616 nm [67] (by adjusting the laser current and grating angle simultaneously at a rate of 10 Hz) excites transitions to the $^1D[5/2]_{5/2}$ state, which decays back to the $^2D_{3/2}$ state. The 398.9-, 638.6-, and 935.2-nm laser systems are constructed in-house in the Littrow configuration.

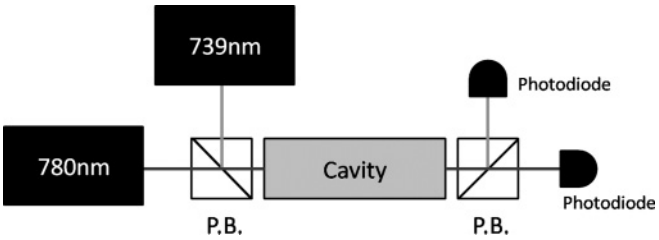

FIG. 5. Pictorial representation of the optical setup for a scanning confocal cavity. The lasers are combined using a polarizing beam splitter and aligned into the cavity. The exiting light is then separated with another polarizing beam splitter onto two photodiodes. Photodiode signals are sampled using a National Instruments analog input sampling card (National Instruments; PCI-6143).

Efficient cooling and repumping require that the lasers are frequency stabilized to within the linewidth of the respective transitions. The 739.05- and 935.2-nm lasers are locked to a stabilized 780-nm laser using a transfer cavity locking scheme [77]. The 780-nm laser, locked to the ^{87}Rb D_2 transition to <1-MHz accuracy, is directed into two scanning confocal Fabry-Perot cavities, each with a finesse of 134(5) and free spectral ranges of 1 GHz and 750 MHz for the 780/739- and 780/935-nm cavities, respectively. The 739.05- and 935.2-nm lasers are then each directed into one of these cavities. Figure 5 illustrates the scheme for the 739.05-nm laser. The resonance peaks from the cavity are read into a computer using an analog input card (National Instruments PCI-6143). The cavities are scanned over 4 GHz at a rate of 100 Hz and, combined with the sample rate of the input card, produce a resolution of 3 MHz, so peaks with FWHMs of 40 MHz consist of $\approx$15 samples. Using LabVIEW Realtime the free spectral range of the 780-nm peaks, a, is compared to the separation of 780- and 739.05-nm (935.2-nm) resonance peaks, b, as shown in Fig. 6. A change in the ratio generates an error signal which is sent, via an NI PCI-6722 analog output card, to the piezo controlling the grating angle on the 739.05-nm (935.2-nm) laser. Feeding back to the cavity piezos to hold the position of the first peak constant with respect to the scan voltage stabilizes the cavity length and removes the requirement for thermal isolation. This technique allows wavelengths to be tuned over a range of $\approx$500 MHz via computer control.

To drift compensate the 398.91- and 638.6-nm lasers the wavelengths are measured (High Finesse WS7; accurate to 60 MHz) and read into a LabVIEW program. The program generates error signals that are sent to the lasers, via the output card (National Instruments; PCI-6722), maintaining the wavelengths.

The stabilized lasers are aligned in the trap as illustrated in Fig. 7. The 398.91- and 369.5-nm beams, with powers of

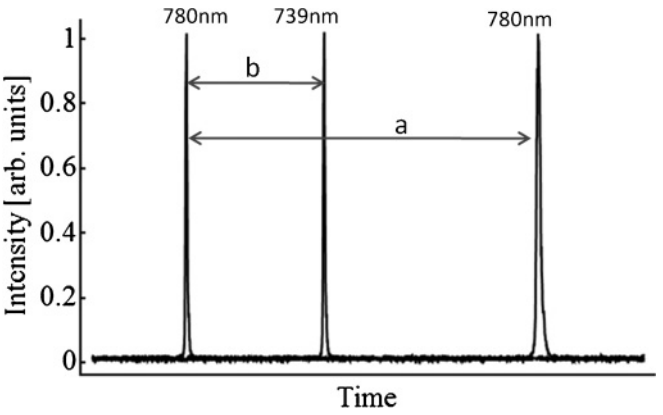

FIG. 6. Combined signal from both photodiodes. The free spectral range of the 780-nm reference laser, a, is measured, as well as the separation between the first 780-nm peak and the first 739.05-nm peak, b. These times are compared and the resulting ratio is maintained to stabilize the 739.05-nm laser.

≈500 μW and ≈1 mW, respectively, are focused to beam waists of 30(5) μm. The higher powers of the 638.6- and 935.2-nm beams, ≈7 mW each, allow for wider foci of 60(5) μm, while maintaining sufficiently high beam intensities. The beam polarizations are oriented at 45° with respect to a 0.5-mT externally applied magnetic field (defining the quantization axis) to couple all Zeeman hyperfine levels to the cooling cycle.

Ions are detected by measuring fluorescence using either an electron multiplied CCD array (EMCCD; Andor iXon885) or a photo multiplier tube (Hamamatsu H8259-01). The device chosen depends on the experiment being performed, the desired detection accuracy, and whether spatial resolution is required.

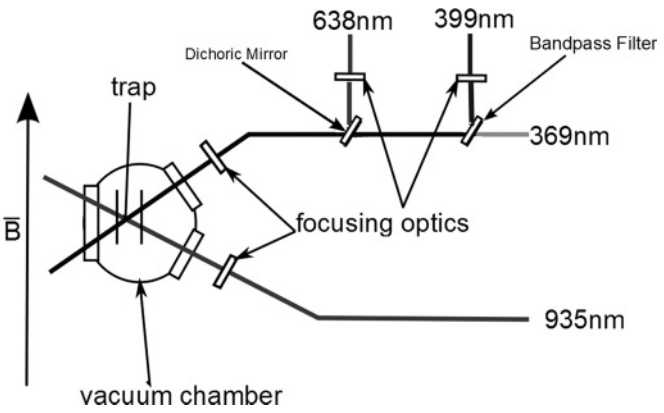

FIG. 7. Diagram showing basic laser setup to provide a good overlap of all four laser beams through the trapping center. A bandpass filter (Semrock; FF01-370/36-25) is used to combine the 369.5- and 398.9-nm beams, which are then combined with the 638.6-nm beam using a dichroic mirror. Also shown is the 0.5-mT applied magnetic field, used to define the quantization axis. For ^{171}Yb$^+$ the lasers are polarized at oblique angles to the quantization axis to avoid potential dark states.

TABLE II. Voltages applied to the trap electrodes, numbered in Fig. 3.

Electrode	Voltage (V)
1	148.88(1)
2	7.36(1)
3	25.03(1)
4	0.00(1)
5	0.00(1)
6	167.76(1)
Compensation 1	169.22(1)
Compensation 2	169.22(1)
Compensation 3	−2.70(1)
rf	680(10)

III. ION TRAP PERFORMANCE

With this experimental setup we can trap single ions and ion crystals of most of the stable Yb$^+$ isotopes, including ^{171}Yb$^+$. To trap ions the static and rf voltages shown in Table II are applied to the electrodes, corresponding to the numbered electrodes in Fig. 3, along with an rf drive signal with a frequency of $\Omega/2\pi = 21.48$ MHz.

The ion secular frequencies, $(\omega_x, \omega_y, \omega_z)/2\pi$, are measured to be $(2.069, 2.110, 1.030) \pm 0.001$ MHz, respectively. They are found by applying an ac voltage to one of the end-cap electrodes and scanning its frequency. When equal to one of the secular frequencies, the ion is resonantly heated, leading to a visible decrystallization. Using these measured secular frequencies, along with electric field simulations [33], the trap depth is determined to be 4.9(2) eV. Ion lifetimes of many hours, without optical cooling, have been observed, and ion crystals, as shown in Fig. 8, can be produced. Figure 8(a) shows a three-ion crystal; Fig. 8(b), a multi-isotope crystal highlighting the potential for many isotope experiments such as sympathetic cooling; and Fig. 8(c), a zigzag ion crystal.

IV. FREQUENCY MEASUREMENTS

Using trapped Yb$^+$ ions the exact cooling and repumping wavelengths are determined. The wavelengths required to excite the neutral $^1S_0 \leftrightarrow {}^1P_1$ transition, creating Yb$^+$ ions, are determined using the fluorescence spot method described in [78]. The Doppler cooling and repumping wavelengths

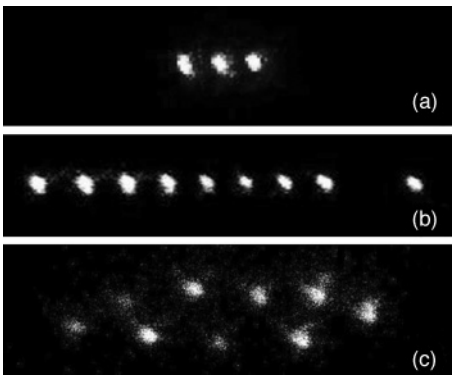

FIG. 8. Crystal of (a) three Yb$^+$ ions, (b) a multi-ion chain of mixed species, and (c) a zigzag structure of nine Yb$^+$ ions

TABLE III. Yb transition wavelengths (vacuum). The neutral atom $^1S_0 \leftrightarrow {}^1P_1$ transition wavelengths apply to our setup where the neutral atomic beam and the laser beam make an angle of 63°. The $^2S_{1/2} \leftrightarrow {}^2P_{1/2}$ and $^2D_{3/2} \leftrightarrow {}^3D[3/2]_{1/2}$ transition wavelengths were obtained by observing fluorescence from a trapped ion. $^{171}Yb^+$ wavelengths correspond to the $^2S_{1/2}(F=1) \leftrightarrow {}^2P_{1/2}(F=0)$ and $^2D_{3/2}(F=1) \leftrightarrow {}^3D[3/2]_{1/2}(F=0)$ transitions, respectively.

Isotope	$^1S_0 \leftrightarrow {}^1P_1$ transition wavelength (nm)	$^2S_{1/2} \leftrightarrow {}^2P_{1/2}$ transition wavelength (nm)	$^2D_{3/2} \leftrightarrow {}^3D[3/2]_{1/2}$ transition wavelength (nm)
$^{170}Yb^+$	398.91051(6)	369.52364(6)	935.19751(20)
$^{171}Yb^+$	398.91070(6)	369.52604(6)	935.18768(20)
$^{172}Yb^+$	398.91083(6)	369.52435(6)	935.18736(20)
$^{174}Yb^+$	398.91114(6)	369.52494(6)	935.17976(20)
$^{176}Yb^+$	398.91144(6)	369.52550(6)	935.17252(20)

are determined by scanning the wavelength of the respective laser while monitoring the ion fluorescence and measuring the wavelength on a wavemeter (High Finesse; WS7). The intensities of the 369.5- and 935.2-nm beams are reduced to 0.4 W cm^{-2} and 0.02 W cm^{-2}, respectively, to reduce the effects of power broadening and the ac Stark shift on the states. The $^2S_{1/2} \leftrightarrow {}^2P_{1/2}$ transition wavelengths are determined as the wavelength just before the fluorescence rapidly drops to background level, corresponding to heating of the ion, and the $^2D_{3/2} \leftrightarrow {}^3D[3/2]_{1/2}$ transition wavelengths are determined as the wavelengths at which maximum fluorescence is obtained. For the even isotopes, the external static magnetic field was removed, while for $^{171}Yb^+$ a magnetic field of 0.5 mT was applied to the ion to remove degeneracy within the hyperfine states, but keep the Zeeman shifts at a manageable level. Table III reports the ionizing, cooling, and repumping wavelengths (vacuum) for the different Yb isotopes. Our measured 369.5-nm cooling wavelengths are in good agreement with those published by E. W. Streed *et al.* [71] who, using a Yb^+ hollow cathode lamp, observed a broadened Doppler absorption line at 369.525 nm, with a width of ≈3 GHz, containing overlapping lines from the multiple ytterbium isotopes. However, our measurements are more precise. The intersection angle between the 398.9-nm laser beam and the average atomic velocity along the atomic beam result in a Doppler shift on the transition wavelength. In our setup the beam of neutral atoms and the 398.9-nm laser beam formed an angle of 63^o, while ionization wavelengths corresponding to different angles are given in Ref. [78]. Due to the infrequent population, precise transition wavelengths for the $^2F_{7/2} \leftrightarrow {}^1D[5/2]_{5/2}$ transition are difficult to obtain. Applying 120 W cm^{-2} to the ion, using wavelengths of 638.618 nm for the even isotopes, and scanning between 638.610 and 638.616 nm for $^{171}Yb^+$ to account for hyperfine states [67], no obvious fluorescence interrupts were observed, indicating that these values are reasonably close to the exact transition wavelengths.

We have carried out a comprehensive error analysis and identify the most significant source of error to be the absolute accuracy of the wavemeter. To eliminate any systematic offsets associated with the wavemeter, it is calibrated using a 780-nm laser, which is locked to <1 MHz of the ^{87}Rb D_2 line, and an additional He-Ne laser (calibrated to <1 MHz) is used to confirm the calibration. The wavemeter is calibrated before the measurements and the frequency standard is remeasured after the measurement to provide further confirmation of the calibration. The absolute accuracy of the wavemeter is specified to be 200 MHz below 370 nm and 60 MHz between 370 and 1100 nm, so the 369.5-nm wavelengths are inferred by measuring the wavelength of the 739.05-nm beam and doubling the frequency, resulting in an error of 120 MHz.

The intensity of the 369.5-nm beam is expected to broaden and ac Stark shift the $^2S_{1/2} \leftrightarrow {}^2P_{1/2}$ transition by 40 MHz and 38 MHz, respectively. As this transition is used for Doppler cooling, blue detuning the laser from the resonant transition frequency results in ion heating and an immediate drop in fluorescence, therefore allowing linewidth broadening to be neglected for these measurements. Fortunately, the resonance frequencies for this transition are determined by the immediate drop in fluorescence at the center of resonance and, so, is independent of linewidth broadening. Repeating the measurements at an intensity of 0.8 Wcm^{-2} yields the same results. The intensity of the 935 nm beam broadens the transition to 30 MHz, and the ac Stark shift is 17 MHz. In addition to the ac Stark shift, the Zeeman shifts are also assessed. The magnetic field is removed for measurements of the even isotopes, leaving the ions exposed to low magnetic fields (such as that from the Earth), inducing a shift of only ≈1 MHz. The 0.5-mT external magnetic field applied when measuring $^{171}Yb^+$ is estimated to change the $\Delta m_F = \pm 1$ transitions by ≈±10 MHz, while transition wavelengths between the magnetic field-insensitive, $m_F = 0$, states are not expected to change. Reducing the magnetic field to 0.25 mT reduced the $\Delta m_F = \pm 1$ transitions by ≈±5 MHz, but due to the relatively large uncertainty associated with the wavemeter, no observable change in the resonance wavelengths was measured. Considering these effects, the overall uncertainty for the $^2S_{1/2} \leftrightarrow {}^2P_{1/2}$ transition wavelengths is ±126 MHz, while the uncertainty for the $^2D_{3/2} \leftrightarrow {}^3D[3/2]_{1/2}$ transition wavelengths is ±70 MHz.

V. HEATING RATE MEASUREMENT

The ion heating rate was measured using a technique proposed by J. H. Wesenberg *et al.* [51]. A $^{174}Yb^+$ ion is trapped and allowed to heat by removing the 369.5-nm cooling beam, using an AOM (Isomet 1212-2-949; response time ≈100 ns), for periods of 1, 3, 5, and 7 s. The cooling laser is turned on again and the fluorescence is measured in 50-μs bins for 4 ms. The particular technique requires the ion energy change to be dominated by heating along one of the principle axes of the trap. Assuming that the heating rate has a $1/\omega^2$ dependence [48], trap secular frequencies of $(\omega_x,\omega_y,\omega_z)/2\pi = (2.069, 2.110, 0.178) \pm 0.001$ MHz result in dominant heating along the z axis.

Heating increases the ion's velocity v, and the instantaneous Doppler shift during an oscillation is $\Delta_D = -kv$, where k is the laser beam wave vector. We define Δ_{max} as the maximum instantaneous Doppler shift Δ_D. The likelihood of the ion experiencing a specific instantaneous Doppler shift is described using a probability density $P_D(\Delta_D)$ [51], and the overlap of $P_D(\Delta_D)$ with the broadened FWHM transition linewidth L

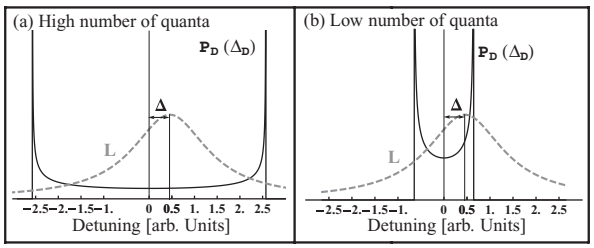

FIG. 9. Overlap of the probability density of the Doppler shift, $P_D(\Delta_D)$ (solid line) with the transition linewidth L (dashed line). (a) Diagram showing the case for a hot ion, with a maximum Doppler shift greater than the broadened transition linewidth and laser detuning, $\Delta_{max} \gg |L| + |\Delta|$. The overlap of both functions is low, leading to a low scatter rate. (b) Diagram showing the case for a cold ion with less energy. The peaks of $P_D(\Delta_D)$ move closer together, resulting in a stronger overlap and an increase in scatter rate.

affects the scatter rate as shown in Fig. 9. Figure 9(a) shows the situation for a hot ion with $\Delta_{max} \gg |L| + |\Delta|$, where Δ is the laser detuning from resonance. Here the Doppler shift probability density and transition linewidth overlap poorly, resulting in low absorption and scatter rates. Figure 9(b) shows the effects of a cold ion, where the probability density overlaps well with the transition linewidth, producing an increased scatter rate.

The relative change in ion energy over one oscillation is small compared to the total energy change during the whole recooling experiment, allowing the energy over an oscillation, and hence the scatter rate, to be averaged. The average scatter rate $\langle dN/dt \rangle$ over one oscillation is [51]

$$\left\langle \frac{dN}{dt} \right\rangle = \int \frac{dN}{dt} P_D(\Delta_D) d\Delta_D, \tag{1}$$

where dN/dt is the instantaneous scatter rate. In the regime of a hot ion, as depicted in Fig. 9(a), the probability density $P_D(\Delta_D)$ is effectively uniform over the transition linewidth. The probability density can be factored out and allows the average scatter rate over one oscillation to be re-expressed in terms of the ion energy as

$$\left\langle \frac{dN}{dt} \right\rangle (E(E_0,t)) = \frac{1}{\sqrt{E(E_0,t)}} \frac{sL^2}{2\sqrt{\frac{2}{m}} k_z (1+s)^{3/2}}, \tag{2}$$

where $E(E_0,t)$ is the ion energy at time t, E_0 the ion energy just before recooling, m the ion mass, k_z the z component of the laser beam vector, s the saturation intensity parameter, and L the broadened transition linewidth. A one-dimensional (1D) Maxwell-Boltzmann distribution is used to describe the thermal distribution of the ion energy before recooling, E_0. The average scatter rate for an ion at time t is [51]

$$\left\langle \frac{dN}{dt} \right\rangle_{E_0} = \int_0^\infty P_B(E_0) \left\langle \frac{dN}{dt} \right\rangle (E(E_0,t))\, dE_0, \tag{3}$$

where $P_B(E_0)$ is the 1D Maxwell-Boltzmann distribution [51]. For the experiment, $\Delta = 6(2)$ MHz, $s = 1.0(2)$, and the observed transition linewidth, $L = 40(5)$ MHz, is suspected to be due to power broadening and micromotion. The z component of the laser beam wave vector is $k_z = 0.45k$. To account for the thermal distribution of E_0, the recooling

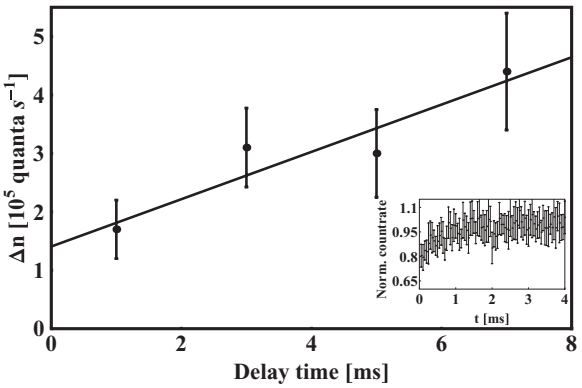

FIG. 10. Change in ion energy in terms of motional quanta, n, after heating periods of 1, 3, 5, and 7 s. Each point results from 500 measurements. Inset: Change in fluorescence during the initial stages of recooling as a function of time.

process was repeated 500 times and averaged. Fitting Eq. (3) to the average fluorescence curve determines the ion energy at the start of recooling.

The ion energy is converted into motional quanta ($\langle n \rangle = E/\hbar\omega_z$), and the change in motional quanta after different delay periods is shown in Fig. 10. The inset shows the averaged fluorescence curve from 500 recooling cycles for a 5-s delay time. Repeating the experiment at secular frequencies of $\omega_z/2\pi = (178,287,355) \pm 1$ kHz produces the plot shown in Fig. 11, which is consistent with the expected $1/\omega^2$ dependence of $\dot{n}$. The cause of ion heating is the electric-field noise density $S_E(\omega_z)$, which is related to the heating $\langle \dot{n} \rangle$ [48,49] via

$$\langle \dot{n} \rangle = \frac{q^2}{4m\hbar\omega_z} S_E(\omega_z), \tag{4}$$

where q is the ion charge, and m the ion mass.

Assuming a $1/\omega^2$ dependency of $\dot{n}$, we calculate $S_E(1\text{ MHz}) = 3.6(9) \times 10^{-11}$ V^2 m^{-2} Hz^{-1}. Considering the ion electrode spacing of 310 μm in our ion trap, the result is consistent with previously measured values of S_E in other ion traps at room temperature [79]. This heating measurement, the first for an ytterbium ion in such a small ion trap structure, has

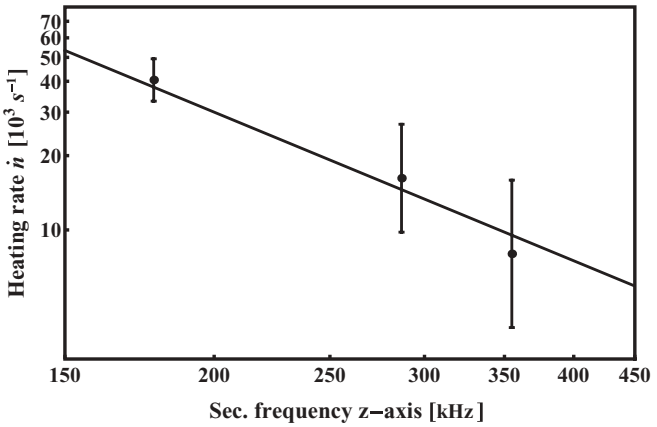

FIG. 11. Heating rate as a function of secular frequency. Heating measurements at secular frequencies of $\omega_z/2\pi = (178,287,355) \pm 1$ kHz are consistent with a $1/\omega^2$ dependence of the trap heating rate.

mitigated a concern that electrodes coated with small amounts of ytterbium may lead to abnormally high heating rates. It is an encouraging result for the use of Yb^+ ions in quantum information processing.

VI. CONCLUSION

We have shown how to create an experimental setup for the operation and development of advanced ion trap chips. In recent years the development of such ion trap designs has gained momentum rapidly, and our setup allows for the simple and reliable operation and testing of such traps. This detailed description of the setup may therefore be very useful for the development of integrated ion chips. An ion trap was operated in this setup and we characterized its performance including a measurement of the motional heating rate. This measurement is consistent with previously reported rates of other ion species in different ion traps using established scaling laws [44,48–50]. It further solidifies the suitability of the Yb^+ ion for quantum information processing, as no abnormally high heating rates are observed in a relatively small ion trap. We also performed wavelength measurements for the $^2S_{1/2} \leftrightarrow {}^2P_{1/2}$ and $^2D_{3/2} \leftrightarrow {}^3D[3/2]_{1/2}$ transitions which are more precise than previous measurements. These measurements are particularly useful for groups setting up an ytterbium ion trap experiment, as the availability of more precise frequency measurements significantly simplifies the initial trapping process.

ACKNOWLEDGMENTS

We would like to thank undergraduate project students Daniel Brown, Nicholas Davies, Jessica Grove-Smith, Ben Pruess, Rajiv Ramasawmy, James Sayers, David Scrivener, Tim Short, and Philippa Young for their work in designing and building various components of the experimental setup. This work was supported by the UK Engineering and Physical Sciences Research Council (Grants No. EP/E011136/1 and EP/G007276/1), the European Commission's Sixth Framework Marie Curie International Reintegration Programme (Grant No. MIRG-CT-2007-046432), the Nuffield Foundation, and the University of Sussex.

[1] J. I. Cirac and P. Zoller, Phys. Rev. Lett. **74**, 4091 (1995).
[2] D. J. Wineland, C. Monroe, W. M. Itano, D. Leibfried, B. E. King, and D. M. Meekhof, J. Res. Natl. Inst. Stand. Technol. **103**, 259 (1998).
[3] H. Häffner, C. F. Roos, and R. Blatt, Phys. Rep. **469**, 155 (2008).
[4] M. Pons, V. Ahufinger, C. Wunderlich, A. Sanpera, S. Braungardt, A. Sen(De), U. Sen, and M. Lewenstein, Phys. Rev. Lett. **98**, 023003 (2007).
[5] A. Friedenauer, H. Schmitz, J. T. Glueckert, D. Porras, and T. Schaetz, Nature Phys. **4**, 757 (2008).
[6] M. Johanning, A. F. Varón, and C. Wunderlich, J. Phys. B **42**, 154009 (2009).
[7] R. J. Clark, T. Lin, K. R. Brown, and I. L. Chuang, J. Appl. Phys. **105**, 013114 (2009).
[8] K. Kim, M.-S. Chang, S. Korenblit, R. Islam, E. E. Edwards, J. Freericks, G.-D. Lin, L. Duan, and C. Monroe, Nature (London) **465**, 590 (2010).
[9] Th. Udem, S. A. Diddams, K. R. Vogel, C. W. Oates, E. A. Curtis, W. D. Lee, W. M. Itano, R. E. Drullinger, J. C. Bergquist, and L. Hollberg, Phys. Rev. Lett. **86**, 4996 (2001).
[10] S. A. Webster, P. Taylor, M. Roberts, G. P. Barwood, and P. Gill, Phys. Rev. A **65**, 052501 (2002).
[11] C. Tamm, S. Weyers, B. Lipphardt, and E. Peik, Phys. Rev. A **80**, 043403 (2009).
[12] M. Chwalla, J. Benhelm, K. Kim, G. Kirchmair, T. Monz, M. Riebe, P. Schindler, A. S. Villar, W. Hänsel, C. F. Roos, R. Blatt, M. Abgrall, G. Santarelli, G. D. Rovera, and Ph. Laurent, Phys. Rev. Lett. **102**, 023002 (2009).
[13] T. Schaetz, M. D. Barrett, D. Leibfried, J. Britton, J. Chiaverini, W. M. Itano, J. D. Jost, E. Knill, C. Langer, and D. J. Wineland, Phys. Rev. Lett. **94**, 010501 (2005).
[14] M. Acton, K.-A. Brickman, P. C. Haljan, P. J. Lee, L. Deslauriers, and C. Monroe, Quantum Inf. Comput. **6**, 465 (2006).
[15] C. Wunderlich, T. K. Th. Hannemann, H. Häffner, C. Roos, W. Hänsel, R. Blatt, and F. Schmidt-Kaler, J. Mod. Opt. **54**, 1541 (2007).
[16] A. H. Myerson, D. J. Szwer, S. C. Webster, D. T. C. Allcock, M. J. Curtis, G. Imreh, J. A. Sherman, D. N. Stacey, A. M. Steane, and D. M. Lucas, Phys. Rev. Lett. **100**, 200502 (2008).
[17] A. H. Burrell, D. J. Szwer, S. C. Webster, and D. M. Lucas, Phys. Rev. A **81**, 040302 (2010).
[18] C. A. Sackett, D. Kielpinski, B. E. King, C. Langer, V. Meyer, C. J. Myatt, M. Rowe, Q. A. Turchette, W. M. Itano, D. J. Wineland, and C. Monroe, Nature (London) **404**, 256 (2000).
[19] D. Leibfried, B. DeMarco, V. Meyer, D. Lucas, M. Barrett, J. Britton, W. M. Itano, B. Jelenković, C. Langer, T. Rosenband, and D. J. Wineland, Nature (London) **422**, 412 (2003).
[20] F. Schmidt-Kaler, H. Häffner, M. Riebe, S. Gulde, G. P. T. Lancaster, T. Deuschle, C. Becher, C. F. Roos, J. Eschner, and R. Blatt, Nature (London) **422**, 408 (2003).
[21] J. Chiaverini, D. Leibfried, T. Schaetz, M. D. Barrett, R. B. Blakestad, J. Britton, W. M. Itano, J. D. Jost, E. Knill, C. Langer, R. Ozeri, and D. J. Wineland, Nature (London) **432**, 602 (2004).
[22] K.-A. Brickman, P. C. Haljan, P. J. Lee, M. Acton, L. Deslauriers, and C. Monroe, Phys. Rev. A **72**, 050306(R) (2005).
[23] J. P. Home, M. J. McDonnell, D. M. Lucas, G. Imreh, B. C. Keitch, D. J. Szwer, N. R. Thomas, S. C. Webster, D. N. Stacey, and A. M. Steane, New J. Phys. **8**, 188 (2006).
[24] C. Ospelkaus, C. E. Langer, J. M. Amini, K. R. Brown, D. Leibfried, and D. J. Wineland, Phys. Rev. Lett. **101**, 090502 (2008).
[25] T. Monz, K. Kim, W. Hänsel, M. Riebe, A. S. Villar, P. Schindler, M. Chwalla, M. Hennrich, and R. Blatt, Phys. Rev. Lett. **102**, 040501 (2009).
[26] S. X. Wang, J. Labaziewicz, Y. Ge, R. Shewmon, and I. L. Chuang, Phys. Rev. A **81**, 062332 (2010).
[27] N. Timoney, V. Elman, S. Glaser, C. Weiss, M. Johanning, W. Neuhauser, and C. Wunderlich, Phys. Rev. A **77**, 052334 (2008).
[28] M. A. Rowe, A. Ben-Kish, B. DeMarco, D. Leibfried, V. Meyer, J. Beall, J. Britton, J. Hughes, W. M. Itano, B. Jelenkovic,

C. Langer, T. Rosenbrand, and D. J. Wineland, Quantum Inf. Comput. **2**, 257 (2002).
[29] W. K. Hensinger, S. Olmschenk, D. Stick, D. Hucul, M. Yeo, M. Acton, L. Deslauriers, C. Monroe, and J. Rabchuk, Appl. Phys. Lett. **88**, 034101 (2006).
[30] S. Schulz, U. Poschinger, K. Singer, and F. Schmidt-Kaler, Fortschr. Phys. **54**, 648 (2006).
[31] R. Reichle, D. Leibfried, R. Blakestad, J. Britton, J. Jost, E. Knill, C. Langer, R. Ozeri, S. Seidelin, and D. J. Wineland, Fortschr. Phys. **54**, 666 (2006).
[32] C. E. Pearson, D. R. Leibrandt, W. S. Bakr, W. J. Mallard, K. R. Brown, and I. L. Chuang, Phys. Rev. A **73**, 032307 (2006).
[33] D. Hucul, M. Yeo, W. K. Hensinger, J. Rabchuk, S. Olmschenk, and C. Monroe, Quantum Inf. Comput. **8**, 0501 (2008).
[34] G. Huber, T. Deuschle, W. Schnitzler, R. Reichle, K. Singer, and F. Schmidt-Kaler, New J. Phys. **10**, 013004 (2008).
[35] R. B. Blakestad, C. Ospelkaus, A. P. VanDevender, J. M. Amini, J. Britton, D. Leibfried, and D. J. Wineland, Phys. Rev. Lett. **102**, 153002 (2009).
[36] J. M. Amini, H. Uys, J. H. Wesenberg, S. Seidelin, J. Britton, J. J. Bollinger, D. Leibfried, C. Ospelkaus, A. P. VanDevender, and D. J. Wineland, New J. Phys. **12**, 033031 (2010).
[37] D. Stick, W. K. Hensinger, S. Olmschenk, M. J. Madsen, K. Schwab, and C. Monroe, Nature Phys. **2**, 36 (2006).
[38] J. Chiaverini, R. Blakestadt, J. Britton, J. Jost, C. Langer, D. Leibfried, R. Ozeri, and D. J. Wineland, Quantum Inf. Comput. **5**, 419 (2005).
[39] M. Brownnutt, G. Wilpers, P. Gill, R. C. Thompson, and A. G. Sinclair, New J. Phys. **8**, 232 (2006).
[40] K. R. Brown, R. J. Clark, J. Labaziewicz, P. Richerme, D. R. Leibrandt, and I. L. Chuang, Phys. Rev. A **75**, 015401 (2007).
[41] J. Britton, D. Leibfried, J. Beall, R. B. Blakestad, J. J. Bollinger, J. Chiaverini, R. J. Epstein, J. D. Jost, D. Kielpinski, C. Langer, R. Ozeri, R. Reichle, S. Seidelin, N. Shiga, J. H. Wesenberg, and D. J. Wineland, e-print arXiv:quant-ph/0605170.
[42] G. Huber, T. Deuschle, W. Schnitzler, R. Reichle, K. Singer, and F. Schmidt-Kaler, New J. Phys. **10**, 013004 (2008).
[43] S. Seidelin, J. Chiaverini, R. Reichle, J. J. Bollinger, D. Leibfried, J. Britton, J. H. Wesenberg, R. B. Blakestad, R. J. Epstein, D. B. Hume, W. M. Itano, J. D. Jost, C. Langer, R. Ozeri, N. Shiga, and D. J. Wineland, Phys. Rev. Lett. **96**, 253003 (2006).
[44] J. Labaziewicz, Y. Ge, P. Antohi, D. Leibrandt, K. R. Brown, and I. L. Chuang, Phys. Rev. Lett. **100**, 013001 (2008).
[45] J. Britton, D. Leibfried, J. A. Beall, R. B. Blakestad, J. H. Wesenberg, and D. J. Wineland, Appl. Phys. Lett. **95**, 173102 (2009).
[46] D. R. Leibrandt, J. Labaziewicz, R. J. Clark, I. L. Chuang, R. J. Epstein, C. Ospelkaus, J. H. Wesenberg, J. H. Bollinger, D. Leibfried, D. Wineland, D. Stick, J. Stick, C. Monroe, C.-S. Pai, Y. Low, R. Frahm, and R. E. Slusher, Quantum Inf. Comput. **9**, 0901 (2009).
[47] D. T. C. Allcock, J. A. Sherman, D. N. Stacey, A. H. Burrell, M. J. Curtis, G. Imreh, N. M. Linke, D. J. Szwer, S. C. Webster, and A. M. Steane, New J. Phys. **12**, 053026 (2010).
[48] Q. A. Turchette, D. Kielpinski, B. E. King, D. Liebfried, D. M. Meekhof, C. J. Myatt, M. A. Rowe, C. A. Sackett, C. S. Wood, W. M. Itano, C. Monroe, and D. J. Wineland, Phys. Rev. A **61**, 063418 (2000).
[49] L. Deslauriers, S. Olmschenk, D. Stick, W. K. Hensinger, J. Sterk, and C. Monroe, Phys. Rev. Lett. **97**, 103007 (2006).
[50] J. Labaziewicz, Y. Ge, D. R. Leibrandt, S. X. Wang, R. Shewmon, and I. L. Chuang, Phys. Rev. Lett. **101**, 180602 (2008).
[51] J. H. Wesenberg, R. J. Epstein, D. Liebfried, R. B. Blakestad, J. Britton, J. P. Home, W. M. Itano, J. D. Jost, E. Knill, C. Langer, R. Ozeri, S. Seidelin, and D. J. Wineland, Phys Rev. A **76**, 053416 (2007).
[52] R. J. Epstein, S. Seidelin, D. Leibfried, J. H. Wesenberg, J. J. Bollinger, J. M. Amini, R. B. Blakestad, J. Britton, J. P. Home, W. M. Itano, J. D. Jost, E. Knill, C. Langer, R. Ozeri, N. Shiga, and D. J. Wineland, Phys. Rev. A **76**, 033411 (2007).
[53] M. R. Dietrich, A. Avril, R. Bowler, N. Kurz, J. S. Salacka, G. Shu, and B. B. Blinov, e-print arXiv:0905.2701.
[54] D. Wineland, C. Monroe, W. Itano, B. King, D. Leibfried, D. Meekhof, C. Myatt, and C. Wood, Fortschr. Phys. **46**, 363 (1998).
[55] H. Nägerl, W. Bechter, J. Eschner, F. Schmidt-Kaler, and R. Blatt, Appl. Phys. B **66**, 603 (1998).
[56] D. M. Lucas, C. J. S. Donald, J. P. Home, M. J. McDonnell, A. Ramos, D. N. Stacey, J.-P. Stacey, A. M. Steane, and S. C. Webster, Phil. Trans. R. Soc. A **361**, 1401 (2003).
[57] R. J. Hughes, D. F. V. James, J. J. Gomez, M. S. Gulley, M. H. Holzscheiter, P. G. Kwiat, S. K. Lamoreaux, C. G. Peterson, V. D. Sandberg, M. M. Schauer, C. M. Simmons, C. E. Thorburn, D. Tupa, P. Z. Wang, and A. G. White, Fortschr. Phys. **46**, 329 (1998).
[58] K. Koo, J. Sudbery, D. M. Segal, and R. C. Thompson, Phys. Rev. A **69**, 043402 (2004).
[59] S. A. Schulz, U. Poschinger, F. Ziesel, and F. Schmidt-Kaler, New J. Phys. **73**, 045007 (2008).
[60] B. B. Blinov, L. Deslauriers, P. Lee, M. J. Madsen, R. Miller, and C. Monroe, Phys. Rev. A **65**, 040304(R) (2002).
[61] M. D. Barrett, B. DeMarco, T. Schaetz, V. Meyer, D. Leibfried, J. Britton, J. Chiaverini, W. M. Itano, B. Jelenković, J. D. Jost, C. Langer, T. Rosenband, and D. J. Wineland, Phys. Rev. A **68**, 042302 (2003).
[62] V. Letchumanan, G. Wilpers, M. Brownnutt, P. Gill, and A. G. Sinclair, Phys. Rev. A **75**, 063425 (2007).
[63] A. S. Bell, P. Gill, H. A. Klein, A. P. Levick, C. Tamm, and D. Schnier, Phys. Rev. A **44**, 20 (1991).
[64] C. Balzer, A. Braun, T. Hannemann, C. Paape, M. Ettler, W. Neuhauser, and C. Wunderlich, Phys. Rev. A **73**, 041407(R) (2006).
[65] D. Kielpinski, M. Cetina, J. A. Cox, and F. X. Kärtner, Opt. Lett. **31**, 757 (2006).
[66] S. Olmschenk, K. C. Younge, D. L. Moehring, D. N. Matsukevich, P. Maunz, and C. Monroe, Phys. Rev. A **76**, 052314 (2007).
[67] M. Roberts, P. Taylor, S. V. Gateva-Kostova, R. B. M. Clarke, W. R. C. Rowley, and P. Gill, Phys. Rev. A **60**, 2867 (1999).
[68] P. Gill, G. P. Barwood, H. A. Klein, G. Huang, S. A. Webster, P. J. Blythe, K. Hosaka, S. N. Lea, and H. S. Margolis, Meas. Sci. Technol. **14**, 1174 (2003).
[69] T. Schneider, E. Peik, and C. Tamm, Phys. Rev. Lett. **94**, 230801 (2005).

[70] K. Hosaka, S. A. Webster, P. J. Blythe, A. Stannard, D. Beaton, H. S. Margolis, S. N. Lea, and P. Gill, IEEE Trans. Instrum. Meas. **54**, 759 (2005).
[71] E. W. Streed, T. J. Weinhold, and D. Kielpinski, Appl. Phys. Lett. **93**, 071103 (2008).
[72] W. W. Macalpine and R. O. Schildknecht, Pro. IRE **47**, 2099 (1959).
[73] J. D. Siverns, S. Weidt, and W. K. Hensinger (in preparation).
[74] M. J. Madsen, W. K. Hensinger, D. Stick, J. A. Rabchuk, and C. Monroe, Appl. Phys. B **78**, 639 (2004).
[75] S. Olmschenk, D. Hayes, D. N. Matsukevich, P. Maunz, D. L. Moehring, K. C. Younge, and C. Monroe, Phys. Rev. A **80**, 022502 (2009).
[76] D. Engelke and C. Tamm, Europhys. Lett. **33**, 347 (1996).
[77] W. Z. Zhao, J. E. Simsarian, L. A. Orozco, and G. D. Sprouse, Rev. Sci. Instrum. **69**, 3737 (1998).
[78] A. H. Nizamani, J. J. McLoughlin, and W. K. Hensinger, Phys. Rev. A **82**, 043408 (2010).
[79] J. M. Amini, J. Britton, D. Leibfried, D. J. Wineland, in *Atom Chips*, edited by J. Reichel and V. Vuletic (WILEY-VCH, in press), e-print arXiv:0812.3907v1.